Monthly Notices of the ROYAL ASTRONOMICAL SOCIETY

MNRAS **496,** 4606–4623 (2020) doi:10.1093/mnras/staa1811
Advance Access publication 2020 June 23

A panchromatic spatially resolved analysis of nearby galaxies – II. The main sequence – gas relation at sub-kpc scale in grand-design spirals

L. Morselli [1,2]★ G. Rodighiero,[1,2] A. Enia [1,2] E. Corbelli,[3] V. Casasola,[3,4] L. Rodríguez-Muñoz [1] A. Renzini [2] S. Tacchella [5] I. Baronchelli,[3] S. Bianchi [3] P. Cassata,[1,2] A. Franceschini,[1] C. Mancini [1,2] M. Negrello,[6] P. Popesso[7] and M. Romano [1,2]

[1]*Dipartimento di Fisica e Astronomia, Università di Padova, vicolo dell'Osservatorio 3, I-35122 Padova, Italy*
[2]*INAF – Osservatorio Astrofisico di Padova, vicolo dell'Osservatorio 5, I-35122 Padova, Italy*
[3]*INAF – Osservatorio Astrofisico di Arcetri, Largo E. Fermi 5, I-50125, Firenze, Italy*
[4]*INAF – Istituto di Radioastronomia, Via P. Gobetti 101, I-40129, Bologna, Italy*
[5]*Center for Astrophysics | Harvard & Smithsonian, 60 Garden Str, Cambridge, MA 02138, USA*
[6]*School of Physics and Astronomy, Cardiff University, The Parade, Cardiff CF24 3AA, UK*
[7]*Excellence Cluster Universe, Boltzmann strasse 2, D-85748 Garching bei München, Germany*

Accepted 2020 June 18. Received 2020 June 16; in original form 2020 March 5

ABSTRACT

In this work, we analyse the connection between gas availability and the position of a region with respect to the spatially resolved main-sequence (MS) relation. Following the procedure presented in Enia et al. (2020), for a sample of five face-on, grand design spiral galaxies located on the MS we obtain estimates of stellar mass and star formation rate surface densities ($\Sigma_\star$ and $\Sigma_{\rm SFR}$) within cells of 500 pc size. Thanks to H I 21cm and ^{12}CO(2–1) maps of comparable resolution, within the same cells we estimate the surface densities of the atomic ($\Sigma_{\rm H\,I}$) and molecular ($\Sigma_{\rm H_2}$) gas and explore the correlations among all these quantities. $\Sigma_\star$, $\Sigma_{\rm SFR}$, and $\Sigma_{\rm H_2}$ define a 3D relation whose projections are the spatially resolved MS, the Kennicutt–Schmidt law and the molecular gas MS. We find that $\Sigma_{\rm H_2}$ steadily increases along the MS relation and is almost constant perpendicular to it. $\Sigma_{\rm H\,I}$ is nearly constant along the MS and increases in its upper envelope. As a result, $\Sigma_{\rm SFR}$ can be expressed as a function of $\Sigma_\star$ and $\Sigma_{\rm H\,I}$, following the relation $\log \Sigma_{\rm SFR} = 0.97 \log \Sigma_\star + 1.99 \log \Sigma_{\rm H\,I} - 11.11$. We show that the total gas fraction significantly increases towards the starburst regions, accompanied by a weak increase in star formation efficiency. Finally, we find that $\rm H_2/H\,I$ varies strongly with the distance from the MS, dropping dramatically in regions of intense star formation, where the UV radiation from newly formed stars dissociates the $\rm H_2$ molecule, illustrating the self-regulating nature of the star formation process.

Key words: galaxies: evolution – galaxies: star formation – galaxies: spirals.

1 INTRODUCTION

In the current model of galaxy formation and evolution, stars form in dense clouds of molecular gas, thanks to the interplay of different physical mechanisms (magnetic fields, turbulence, shielding, feedback). Despite its complexity, this interplay translates in tight correlations between different physical quantities: (i) between the surface density of the star formation rate ($\Sigma_{\rm SFR}$) and the surface density of the gas ($\Sigma_{\rm gas}$), and (ii) between the stellar mass surface density ($\Sigma_\star$) and $\Sigma_{\rm SFR}$. The first relation, originally formulated by Schmidt (1959) using the gas volume density and the number of stars formed in the solar neighbourhood, was subsequently derived by Kennicutt (1998) for radially averaged surface densities in external galaxies, and it is thus called the Kennicutt–Schmidt (KS) relation. The second, called main sequence (MS), was initially found using integrated quantities of star-forming galaxies (thus the total SFR and stellar mass $M_\star$) in Brinchmann et al. (2004) for local galaxies and later confirmed for high-redshift galaxies by several works (e.g. Daddi et al. 2007; Elbaz et al. 2007; Noeske et al. 2007; Salim et al. 2007). As both relations are intrinsically related to the process of star formation and thus to galaxy evolution as a whole, and because they are fundamental ingredients of theoretical models and simulations, they have been intensively studied in the past (e.g. Tan 2000; Boissier et al. 2003; Springel & Hernquist 2003; Krumholz & McKee 2005; Rodighiero et al. 2011; Kennicutt & Evans 2012; Krumholz, Dekel & McKee 2012; Whitaker et al. 2012; Kashino et al. 2013; Hopkins et al. 2014; Speagle et al. 2014; Genzel et al. 2015; Schreiber et al. 2015; Kurczynski et al. 2016; Tacchella et al. 2016; Santini et al. 2017; Orr et al. 2018; Pearson et al. 2018; Morselli et al. 2019; Popesso et al. 2019).

The KS law relates the fuel of star formation to its end product, stars; its shape has important effects on the depletion time of the gas ($t_{\rm depl} = M_{\rm gas}/{\rm SFR}$, with $M_{\rm gas}$ the total gas mass), or equivalently on the efficiency of the star formation process (${\rm SFE} = {t_{\rm depl}}^{-1} = {\rm SFR}/M_{\rm gas}$). In one of the earliest works, Kennicutt (1998) finds a super-linear correlation (slope = 1.4–1.5) between the total gas and the SFR surface densities. Following this result, several papers investigate the relation between star formation and gas availability, considering different gas phases and star formation tracers, as well as exploring this

★ E-mail: laura.morselli@unipd.it

link at different cosmic epochs (e.g. Wyder et al. 2009; Genzel et al. 2010; Tacconi et al. 2010; Genzel et al. 2012). Bigiel et al. (2008), Leroy et al. (2008), Leroy et al. (2013), and Schruba et al. (2011) exploit molecular and neutral gas observations of nearby galaxies to investigate how the relation between gas and star formation activity varies within galaxies and as a function of local and integrated properties. Overall, their findings indicate that the connection between star formation and molecular gas is a linear relation (i.e. slope $\sim$1), thus implying a constant molecular SFE and $t_{\rm depl}$ (around 2.2 Gyr). Leroy et al. (2013) find second-order variations in the molecular gas $t_{\rm depl}$ and study how some of them can be related to variations in the $\alpha_{\rm CO}$ conversion factor between CO luminosity and H_2 mass, while further variability might arise as a consequence of galaxy properties. Bigiel et al. (2010), instead, study the relation between recent SF activity and H I outside the optical disc, in regions where H I represents the totality of the ISM, and find significant spatial correlation between FUV (tracing recent dust-unobscured star formation) and H I density. They also find that the SFE ($t_{\rm depl}$) decreases (increases) with increasing radius. Similarly, Roychowdhury et al. (2015) study the spatially resolved KS relation on sub-kpc and kpc scales in the H I-dominated regions of nearby spirals and irregular galaxies and find that gas consumption time-scales are longer compared to H_2-dominated regions (lower SFE). Other works investigated, at earlier cosmic epoch, the spatially resolved (e.g. Freundlich et al. 2013; Genzel et al. 2013) and integrated (Freundlich et al. 2019) KS relation. In particular, Freundlich et al. (2019) obtain a linear galaxy-averaged molecular KS relation, implying that galaxies at different cosmic epochs have similar star formation time-scales. This is consistent with the results of Peng & Renzini (2020), which find that the sSFR (SFR/$M_\star$) and $M_{\rm H_2}/M_\star$ have the same redshift evolution, thus implying a linear KS law. On the other hand, galaxy-to-galaxy variations in the molecular gas–star formation relation have also been reported. For example, Ford et al. (2013), Shetty, Kelly & Bigiel (2013), Shetty, Clark & Klessen (2014b), and Shetty et al. (2014a) find evidence for a sub-linear relation within galaxies and for the combined samples. Also, Casasola et al. (2015) find galaxy-to-galaxy variations of the spatially resolved KS relation, and underline that the slope can be both sub-linear and super-linear, depending on the spatial scale. de los Reyes & Kennicutt (2019) revisit the integrated KS law in local, normal star-forming galaxies and find that spirals lie on a tight log-linear relation with slope 1.41 $\pm$ 0.07 (when considering both the neutral and molecular gas) while dwarfs populate the region below it.

The second fundamental relation, the MS, relates stars that have already formed to the ongoing SFR. The existence of the MS up to $z \sim 4$ (characterized by a non-evolving slope and scatter and an increasing normalization with increasing redshift, e.g. Speagle et al. 2014; Popesso et al. 2019) was interpreted in the framework of gas-regulated galaxy evolution, according to which galaxies grow along the MS thanks to the continuous replenishment of their gas supply (e.g. Dekel et al. 2009; Bouché et al. 2010; Lilly et al. 2013). The observation of outliers located above the MS relation (starburst are generally classified in literature as galaxies having an SFR that is a factor of 4 higher that the MS value at fixed stellar mass, e.g. Rodighiero et al. 2011) at different cosmic epochs sparkled the interest on whether these sources: (i) have larger gas reservoirs [thus a higher gas fraction, $f_{\rm gas} = M_{\rm gas}/(M_{\rm gas} + M_\star)$, e.g. Lee et al. 2017], (ii) are more efficient in converting gas into stars (thus a higher SFE, e.g. Solomon et al. 1997; Daddi et al. 2010; Silverman et al. 2015, 2018; Ellison et al. 2020a), or (iii) a combination of both (e.g. Saintonge et al. 2011a, 2012; Huang & Kauffmann 2014; Scoville et al. 2017; Tacconi et al. 2018). In the recent years, the advent of large integral field spectroscopic (IFS) surveys revealed that the integrated MS relation originates at smaller scales (up to the sizes of molecular clouds), thus implying that the star formation process is regulated by physical process that act on sub-galactic scales (Cano-Díaz et al. 2016; Abdurro'uf & Akiyama 2017; Hsieh et al. 2017; Lin et al. 2017; Hall et al. 2018; Medling et al. 2018; Cano-Díaz et al. 2019; Vulcani et al. 2019; Bluck et al. 2020; Enia et al. 2020). Despite a general consensus on the existence of the spatially resolved MS, the slope, intercept, and scatter of the relation vary significantly among different works, depending on the sample selection, SFR indicator, dust correction, and fitting procedure. Moreover, some authors find that the spatially resolved relation vary dramatically from galaxy to galaxy. Recently, the combination of MaNGA (Mapping Nearby Galaxies at APO, Bundy et al. 2015) and ALMaQUEST (the ALMA-MaNGA QUEnching and STar formation survey) allowed the study of the link between the spatially resolved MS and gas reservoirs and the investigation of the nature of starburst regions within galaxies. By analysing 14 MS galaxies, Lin et al. (2019) suggest that the MS relation originates from two more fundamental relations: the molecular KS and the so-called MGMS, a relation between $\Sigma_\star$ and $\Sigma_{\rm H2}$. Ellison et al. (2020b) exploit 34 galaxies in ALMaQUEST to study the nature of variations in the SFR on kpc scales. They find that while the average SFR is regulated by the availability of molecular gas, the scatter of the spatially resolved MS (and thus variations with respect to the average SFR value) originates in variations of the SFE. Dey et al. (2019), using optical IFU and CO observations collected in the EDGE-CALIFA survey (CARMA Extragalactic Database for Galaxy Evolution Bolatto et al. 2017, see also Barrera-Ballesteros et al. 2020), find that $\Sigma_{\rm SFR}$ is a function of both $\Sigma_\star$ and $\Sigma_{\rm H_2}$, but different from Lin et al. (2019), the relation with the stellar mass is statistically more significant than the one with the molecular gas. Early works on the formation of molecular hydrogen in the ISM, such as Elmegreen (1993) and Blitz & Rosolowsky (2006), have underlined the role of the disc hydrostatic pressure, and hence of $\Sigma_\star$, in promoting the formation of molecules. Also the works of Shi et al. (2011) and Shi et al. (2018), that propose an *extended KS law* expressed as a proportionality between Σ_{SFE} and $\Sigma_\star$, emphasize the role of existing stars in setting the current production of stars, which indeed is the very nature of the MS.

In this paper, we build on the work presented in Enia et al. (2020, hereafter Paper I) and analyse the sub-kpc relation between the surface densities of star formation, gas in different phases, and stellar mass in five local grand-design spirals. In Paper I, we exploit multiwavelength observations in more than 20 photometric bands to obtain spatially resolved estimates of $\Sigma_\star$ and $\Sigma_{\rm SFR}$ on different physical scales, from few hundred parsecs to 1.5 kpc, via SED fitting. We use these estimates to study the spatially resolved MS relation and find the slope to be consistent for different spatial scales, as well as with the slope of the integrated relation. Here, we aim at analysing under which gas properties different spatial regions populate different loci of the spatially resolved MS, thus trying to understand whether the SFR is more connected to the gravity of the disc (dominated by stars up to $\sim$2/3 of the optical radius) or with the availability of fuel, or a combination of both. We exploit observations in more than 20 photometric bands to derive accurate SFR and $M_\star$ maps to compare to H I and H_2 maps. We discuss the origin of the spatially resolved MS, in terms of its slope and scatter.

The structure of the paper is the following. In Section 2, we give a short description of the data used in this work; in Section 3, we present our results at 500 pc resolution; in Section 4, we analyse the implications of our results on the existence of the MS relation and

Table 1. Properties of the galaxies in our sample: (1) galaxy name; (2,3) RA and Dec coordinates in J2000; (4) total $M_\star$ from SED fitting; (5) total SFR computed from equation (1) with L_{UV} and L_{IR} from SED fitting; (6,7) distance in Mpc and radius in kpc at which the optical surface brightness falls below 25 mag arcsec^{-2}, both taken from the HyperLEDA data base; (8) total H I mass in R_{25}; (9) total H_2 mass in R_{25}; (10) morphological T type, taken from HyperLEDA; (11) central metallicity computed using the O3N2 index, and taken from the DustPedia archive.

Galaxy name	RA (deg)	Dec. (deg)	log$M_\star$ ($M_\odot$)	SFR ($M_\odot$ yr^{-1})	D (Mpc)	R_{25} (kpc)	log$M_{H\,I}$ ($M_\odot$)	logM_{H_2} ($M_\odot$)	T	12 + log(O/H)
NGC 0628 (M74)	24.174	15.7833	10.31 ± 0.15	1.78 ± 0.41	10.14	14.74	9.54 ± 0.18	9.39 ± 0.20	5.2	8.693 ± 0.001
NGC 3184	154.5708	41.4244	10.13 ± 0.10	1.02 ± 0.10	11.64	12.55	9.38 ± 0.14	9.20 ± 0.24	5.9	$8.766^{+0.014}_{-0.013}$
NGC 5194 (M51a)	202.8025	47.1952	10.74 ± 0.20	3.68 ± 0.26	8.59	17.23	9.43 ± 0.17	9.86 ± 0.22	4.0	$8.824^{+0.017}_{-0.016}$
NGC 5457 (M101)	210.8025	54.3491	10.37 ± 0.13	3.00 ± 0.15	7.11	24.81	10.15 ± 0.14	9.41 ± 0.18	5.9	$8.528^{+0.006}_{-0.007}$
NGC 6946	308.71905	60.15361	10.61 ± 0.13	3.51 ± 0.15	6.73	24.81	9.41 ± 0.15	9.74 ± 0.17	5.9	$8.746^{+0.067}_{-0.070}$

on how SFE and f_{gas} vary with varying SFR. Finally, in Section 5 we summarize our findings. The assumed IMF is Chabrier (2003), cosmology is ΛCDM with parameters from Planck Collaboration XIII (2016).

2 DATA

This work is based on multiwavelength observations of five nearby face-on spiral galaxies: NGC 0628, NGC 3184, NGC 5194, NGC 5457, and NGC 6946. Four out of five galaxies are in common with Paper I: they are the ones observed in 23 photometric bands, and included in the THINGS and HERACLES surveys. NGC 6946 was initially excluded from the Paper I sample, since it lacked optical observations (the five Sloan optical filters). We tested for the sample in Paper I how the SED fitting routine results change excluding these five photometric points, finding that they are nearly unchanged. Following this, we are including NGC 6946 in this analysis. The observations in 23 different bands (18 for NGC 6946) have been collected in the DustPedia [1] (Davies et al. 2017; Clark et al. 2018) archive; more details on the data set can be found in Paper I and references therein. The main properties of the galaxies in this sample are shown in Table 1. We highlight two properties of our sample: (i) according to the integrated SFR and $M_\star$ values, the objects in our sample are MS galaxies, located within 0.2 dex from the relation obtained in Paper I, and (ii) three out of five sources are classified as SAB spirals (NGC 3184, NGC 5457, and NGC 6946), thus show evidence of a bar component.

2.1 SFRs, stellar mass, and distance from the MS

The spatially resolved measurements at 500 pc resolution of $\Sigma_\star$, Σ_{SFR}, and distance from the MS (Δ_{MS}), have been obtained following the procedure presented in Paper I. Briefly, we select 8 nearby, face-on, grand design spiral MS galaxies with log $M_\star \sim$ 10.4–10.6 $M_\odot$, and perform spatially resolved SED fitting to 23 photometric bands using MAGPHYS (da Cunha, Charlot & Elbaz 2008). In particular, we performed SED fitting on cells having two different side measurements: 8 arcsec (thus a varying physical scale between 290 and 700 pc, depending on the distance of the galaxies) and 1.5 kpc. Here, we implement an improved procedure and performed SED fitting at a common resolution of 500 pc (as discussed in Paper I, these scales are higher than the ones where the energy-balance criterion holds, ∼200–400 pc). The procedural improvements are the following: (i) we estimate the noise on the photometry of each cell from the rms maps (while in Paper I we used the DustPedia photometry signal-to-noise ratio); (ii) if a cell has more than 10 bands with SNR < 2 it is automatically excluded from the SED fitting procedure, thus reducing computational time. These improvements influence the χ^2 estimation in MAGPHYS, increasing the number of accepted points within the optical radius, and leading to cleaner results in the outer part of galaxies, where the photometry is fainter. The slope and intercept of the spatially resolved MS given in Paper I do not change when these improvements are implemented in the pipeline.

In each cell, the SFR is computed as the sum of unobscured (SFR_{UV}) and obscured (SFR_{IR}) star formation activity, obtained using the relations of Bell & Kennicutt (2001) and Kennicutt (1998) (reported to Chabrier IMF):

$$SFR = 0.88 \times 10^{-28} L_{UV} + 2.64 \times 10^{-44} L_{IR}, \quad (1)$$

where L_{UV} and L_{IR} are taken from the best-fitting SED and are the luminosity (in erg s^{-1} Hz^{-1}) at 150 nm and the one (in erg s^{-1}) integrated between 8 and 1000 μm, respectively. As shown in fig. 3 of Paper I, the SFR computed following equation (1) and the one that MAGPHYS gives as output are highly consistent. Here, for consistency with Paper I, we use the SFRs estimated with equation (1), but the results would not change when considering the SFRs given as output of the SED-fitting procedure.

As the sample of galaxies used here differs from the one of Paper I, we decided to recompute the spatially resolved MS for this sample, but following the same procedure, i.e. (1) by fitting with a log-linear relation the median values of logΣ_{SFR} in bins of log$\Sigma_\star$, using EMCEE (Foreman-Mackey et al. 2013) and considering 10 bins in the log$\Sigma_\star$ range [6.5:8.5] $M_\odot$ pc^{-2}, plus an additional bin to include the few points between [8.5:9.5] $M_\odot$ pc^{-2}, and (2) by implementing an orthogonal distance regression (ODR) technique. The slope and intercept of the MS are 0.76(±0.20) and −8.15(±1.63) with the first method, and 0.87(±0.01) and −8.94(±0.06) with the second. These estimates are consistent with the ones in Paper I. In the following analysis we make use of the distance from the MS relation computed with the binning technique, but our results do not change when considering the ODR MS relation.

For each region, we compute the distance from the MS as the difference between log Σ_{SFR} and the MS value (in log) estimated for the $\Sigma_\star$ of the region, thus Δ_{MS} = log Σ_{SFR} − (0.76log $\Sigma_\star$ − 8.15). The left-hand panel of Fig. 1 shows, as an example, the Δ_{MS} map of NGC 0628; cells in red are located below the spatially resolved MS, while the ones in blue are located above the relation (the Δ_{MS} maps of the other galaxies in the sample are shown in Appendix B). Within the optical radius (the dashed circle), we are able to recover most of

[1]The DustPedia data base is available at http://DustPedia.astro.noa.gr.

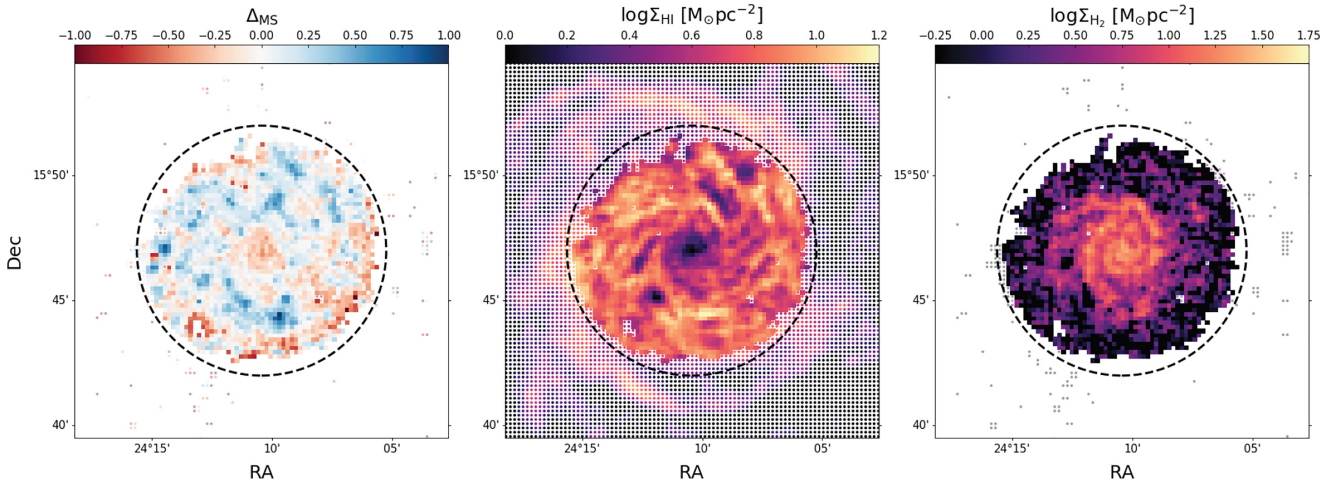

Figure 1. Spatially resolved properties of NGC 0628: Δ_{MS} in the *left-hand panel*, $\log\Sigma_{H\,I}$ in the *central panel*, and $\log\Sigma_{H_2}$ in the *right-hand panel*. The dashed circle has a radius equal to the optical radius of the galaxy, R_{25}. In the left-hand and right-hand panels, small dots are the cells where the SED fitting is characterized by a large χ^2 and are thus rejected. In the central panel, the dotted points are the ones with measured $\log\Sigma_{H\,I}$ but no (or rejected) Δ_{MS}.

the cells, especially at $r < 0.9\ R_{25}$.[2] We emphasize here that the MS relation we obtain is well defined also in the outer parts of the optical disc, where the SFR and $M_\star$ are small in absolute values. We refer the reader to Paper I for details on the SED-fitting procedure, as well as for how the spatially resolved MS relation is obtained.

2.2 Neutral gas: H I 21 cm observations

Neutral hydrogen mass surface densities ($\Sigma_{H\,I}$) are measured from 21cm maps available from the THINGS survey (The H I Nearby Galaxy Survey; Walter et al. 2008). These observations have been carried out with the Very Large Array (VLA) and are characterized by a high angular resolution (6 arcsec and 10 arcsec in the robust and natural weighting, respectively). To compute the H I surface brightness, $\Sigma_{H\,I}$, we first convolve the 21 cm natural-weighted intensity maps, given in Jy beam^{-1} m s^{-1}, to the resolution of the worst of the 23 photometric bands used in the SED fitting (the one of SPIRE350, 24 arcsec, see Paper I) using a Gaussian kernel. We used the beam sizes given in table 2 of Walter et al. (2008) and equation 1 to obtain the flux in K km s^{-1} and then estimate $\Sigma_{H\,I}$ from equation 5 of Walter et al. (2008) (that does not include a correction for helium). We compute the sensitivity limit from our maps of $\Sigma_{H\,I}$ at 500 pc resolution and find $\Sigma_{H\,I,lim} \sim 2\ M_\odot\ pc^{-2}$. The central panel of Fig. 1 shows the distribution of $\Sigma_{H\,I}$ in NGC 0628. As in several other spiral galaxies, the H I is centrally depressed (e.g. Casasola et al. 2017), and it extends on radius that are significantly larger that the optical radius (Swaters et al. 2002; Wang et al. 2013). The values of $M_{H\,I}$ within R_{25} are reported in Table 1. For the galaxies in our sample, the H I gas-to-stellar mass ratio ($M_{H\,I}/M_\star$) within R_{25} varies from 5 per cent to 60 per cent.

2.3 Molecular gas: CO observations

The molecular gas surface density, Σ_{H_2}, is computed using the ^{12}CO(2−1) intensity maps from the HERACLES survey (The HERA CO-Line Extragalactic Survey; Leroy et al. 2009). These observations were made with the IRAM 30 m telescope and have an angular resolution of 11 arcsec. As for $\Sigma_{H\,I}$, we convolve the images using a Gaussian kernel to the resolution of SPIRE350. We estimated Σ_{H_2} using equation 4 of Leroy et al. (2009), considering a metallicity independent conversion factor X_{CO} ($X_{CO} = N(H_2)/I_{CO}$, where $N(H_2)$ is the H_2 column density and I_{CO} is the line intensity) equal to 2×10^{20} cm^{-2}(K km s^{-1})$^{-1}$ (the typical value for disc galaxies, see e.g. Bolatto, Wolfire & Leroy 2013), and a CO line ratio $I_{CO(2-1)}/I_{CO(1-0)} = 0.8$ (e.g. Leroy et al. 2009; Schruba et al. 2011; Casasola et al. 2015). We divide by a factor of 1.36 that is included in equation 4 of Leroy et al. (2009) to remove the helium contribution. In Section 3 we show that the results presented here remain true when considering a metallicity-dependent X_{CO} factor, using the X_{CO}−(12 + log O/H) relation of Genzel et al. (2011) and the spatially resolved metallicity measurements collected in DustPedia. The sensitivity limit, computed as the rms of our $\log\Sigma_{H_2}$ maps at 500 pc resolution, is $\log\Sigma_{H_2,\,lim} = 0.4\ M_\odot\ pc^{-2}$. For the regions corresponding to a negative flux of ^{12}CO(2 − 1), in the $\Sigma_{H_2,\,lim}$ map we replace the value with a randomly generated number between 0 and the sensitivity limit, so that Σ_{H_2} can be computed as an upper limit. While this step does not influence our results concerning H_2, it allows us to extend the analysis also to the regions where H_2 is not detected. The right-hand panel of Fig. 1 shows the distribution of Σ_{H_2} in NGC 0628. The H_2 is centrally concentrated, and mostly below the sensitivity limit for $r > 0.5R_{25}$. For the galaxies in our sample, the H_2 gas-to-stellar mass ratio ($M_{H_2}/M_\star$) within R_{25} is almost constant around 11–14 per cent.

3 RESULTS

Before analysing the spatially resolved connection between star formation and gas components, we briefly comment on the integrated properties of the galaxies in our sample. It is worth underlying that, within R_{25}, three out of five galaxies have similar amount of neutral and molecular gas (M_{H_2} and $M_{H\,I}$), within the uncertainties. This is consistent with the results of Casasola et al. (2020), as they find that, within R_{25}, galaxies with morphological type $T = 4, 5, 6$ have $M_{H_2}/M_{H\,I} = 0.91$, 1, and 1.05, respectively. For NGC 5457 and NGC

[2] R_{25} is defined as the length of the projected semimajor axis of a galaxy at the isophotal level 25 mag arcsec^{-2} in the *B* band and it is taken from the HyperLEDA data base (Makarov et al. 2014).

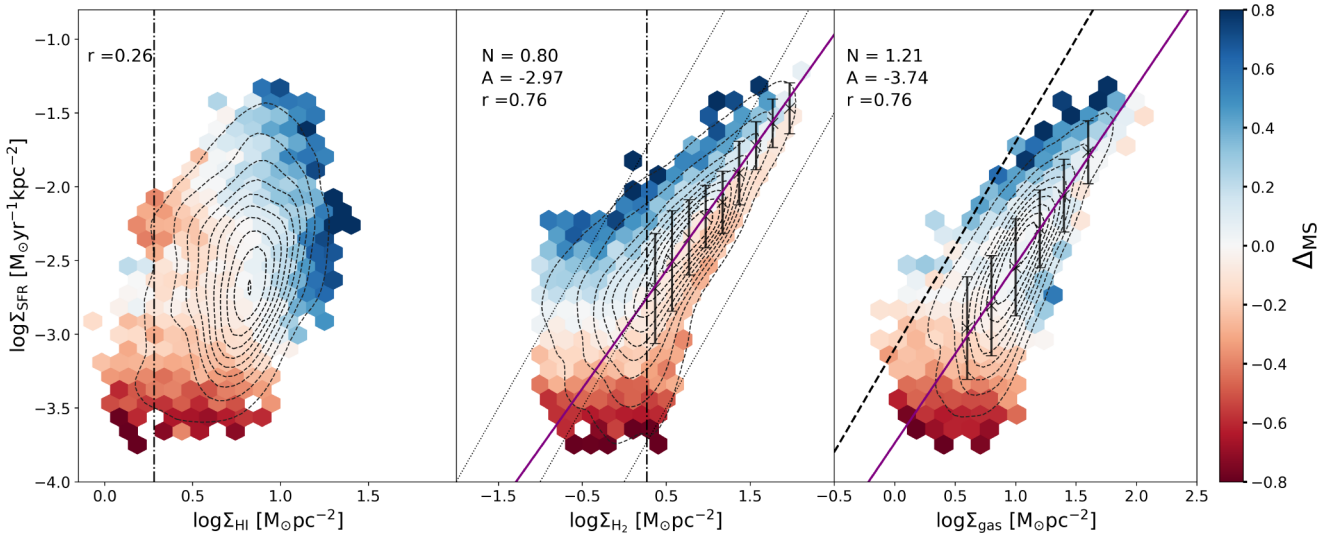

Figure 2. Relations between Σ_{SFR} and $\Sigma_{H\,I}$ (left-hand panel), Σ_{H_2} (middle panel), and Σ_{gas} (for the total H I+H_2 gas, right-hand panel) colour coded as a function of the median value of Δ_{MS} in each bin. Only bins containing a minimum number of three cells are shown in the plot. The dashed contours encircle the areas of the plane containing from 10 per cent to 90 per cent of the data, at steps of 10 per cent. The sensitivity limits are represented by the dot–dashed black lines. The purple solid lines in the middle and right-hand panel represent the best fit to the data obtained fitting the points marked with crosses; the corresponding slope (*N*) and intercept (*A*) are written in the panels, together with the Spearman correlation coefficient *r*.
In the central panel, the dotted lines mark constant molecular t_{depl} of 10^8, 10^9, and 10^{10} yr from top to bottom. In the right-hand panel, the dashed black line is the fit to local ULIRGs and SMGs taken from Daddi et al. (2010).

5194, the average value associated with their morphological type does not describe well their gas properties. It is well know that NGC 5457 is likely to have experienced a recent event of gas accretion (Mihos et al. 2013; Vílchez et al. 2019) which can explain the H I rich outer disc and its high total H I mass. A high molecular gas mass fraction, as for NGC 5194, is likely the result of tidal stirring by a companion.

3.1 Dependency of the SFR on gas

With the data set in our hands, we first investigate the spatially resolved relations between the SFR and the different gas phases, by analysing how Σ_{SFR} relates to $\Sigma_{H\,I}$, Σ_{H_2}, and Σ_{gas}. This last quantity is computed as the sum of the neutral and molecular component for all the regions where the Σ_{H_2} is above the sensitivity limit, while it is equal to Σ_{H_I} otherwise, and it is thus a lower limit. The results of this exercise are shown in Fig. 2.

As expected, no significant correlation is found between Σ_{SFR} and $\Sigma_{H\,I}$ (Spearman correlation coefficient $r = 0.26$), while tight correlations are present between Σ_{SFR} and Σ_{H_2}, and Σ_{SFR} and Σ_{gas} ($r = 0.76$), confirming several results in the literature (e.g. Bigiel et al. 2008; Kumari, Irwin & James 2020). In Fig. 2, we add the information on how regions located at different distance from the spatially resolved MS populate the $\log\Sigma_{SFR} - \log\Sigma_{H\,I/H_2/gas}$ plane. To do so, we divide the $\log\Sigma_{SFR}$–$\log\Sigma_{H\,I/H_2/gas}$ planes in bins colour coded according to the median value of Δ_{MS} in each bin. We observe that regions above the MS are found in correspondence to the highest $\Sigma_{H\,I}$, but span a wide range of Σ_{H_2} values. Analogously, regions located below the MS are preferentially found at lower $\Sigma_{H\,I}$, while are characterized by Σ_{H_2} spanning the whole range of possible values. For $\log\Sigma_{SFR} > -2$, the trend between $\log\Sigma_{H\,I}$ and Δ_{MS} is less evident; this is due to the fact that we are not well sampling the region below the MS, as shown in fig. 5 of Paper I, and confirmed by the decrease of the scatter of the spatially resolved MS at the higher stellar surface densities. Analogously, the points with $\log\Sigma_{SFR} < -3$ are mostly found on the MS or below it, thus hiding a possible trend at the lowest SFRs. When considering the total gas, we see that regions closer to the relation that describes local Ultra-Luminous IR Galaxies (ULIRGs) and sub-mm galaxies (dashed black lines, taken from Daddi et al. 2010) are the ones located above the relation. On the other hand, the general behaviour between the distance from the best-fitting relation and the distance from the MS is less regular than in the case of molecular gas. Indeed, the central panel of Fig. 2 suggests that the spatially resolved MS is intrinsically linked to the molecular gas–SFR relation, as MS regions (in white) fall very consistently along the $\log\Sigma_{SFR}$–$\log\Sigma_{H_2}$ relation. Regions that populate the upper (lower) envelope of the molecular KS law are also found in the upper (lower) envelope of the spatially resolved MS relation. This is qualitatively consistent with what found by Ellison et al. (2020b) when analysing the molecular gas–SFR relation exploiting ALMA and MaNGA data on kpc scales.

By fitting the average values of $\log\Sigma_{SFR}$ in bins of $\log\Sigma_{H_2}$ and $\log\Sigma_{gas}$ (both above the sensitivity limit of $\log\Sigma_{H_2}$), we find the following scaling relations (slopes *N* and intercepts *A* are also written in the corresponding panels):

$$\log \Sigma_{SFR} = 0.80(\pm0.12) \times \log \Sigma_{H_2} - 2.97(\pm0.85) \quad (2)$$

and

$$\log \Sigma_{SFR} = 1.21(\pm0.18) \times \log \Sigma_{gas} - 3.74(\pm1.15) \quad (3)$$

The two correlations have equal strength according to the Spearman coefficient, and their scatter is in both cases smaller than the one of the spatially resolved MS: 0.19 for the $\log\Sigma_{H_2}$–$\log\Sigma_{SFR}$ relation and 0.17 for the $\log\Sigma_{gas}$–$\log\Sigma_{SFR}$. The relation between $\log\Sigma_{SFR}$ and $\log\Sigma_{H_2}$ is sub-linear, but becomes linear when the ODR fitting is applied. We retrieve a molecular t_{depl} that varies between 1.6 and 3 Gyr. These results are in agreement with the typical t_{depl} in normal spiral galaxies (see e.g. Bigiel et al. 2008; Saintonge et al. 2011b; Leroy et al. 2013; Casasola et al. 2015). It is worth noticing that the slope of the spatially resolved KS relation obtained from

Table 2. Slope, intercept, and scatter of the following relations: molecular KS law, log Σ_{gas}–log Σ_{SFR}, MGMS, and log $\Sigma_\star$–log Σ_{gas}. We list the best-fitting parameters for log Σ_{H_2} computed using a constant XCO factor and a metallicity dependent XCO obtained from estimates of the metallicity that use (1) the N2 index and (2) the O3N2 index.

Correlation	Slope			Intercept			Scatter		
	Const α_{CO}	O3N2	N2	Const α_{CO}	O3N2	N2	Const α_{CO}	O3N2	N2
log Σ_{H_2}–log Σ_{SFR}	0.80 ± 0.12	0.83 ± 0.12	0.83 ± 0.11	−2.97 ± 0.87	−2.97 ± 0.93	−2.94 ± 0.94	0.19	0.20	0.19
log Σ_{gas}–log Σ_{SFR}	1.21 ± 0.18	1.24 ± 0.16	1.25 ± 0.18	−3.74 ± 1.15	−3.74 ± 1.15	−3.73 ± 1.14	0.17	0.18	0.18
log $\Sigma_\star$–log Σ_{H_2}	0.91 ± 0.29	0.84 ± 0.29	0.87 ± 0.27	−6.15 ± 2.11	−5.66 ± 2.12	−5.93 ± 2.07	0.22	0.24	0.23
log $\Sigma_\star$–log Σ_{gas}	0.50 ± 0.14	0.49 ± 0.14	0.49 ± 0.13	−2.64 ± 0.97	−2.62 ± 1.08	−2.72 ± 1.05	0.24	0.25	0.25

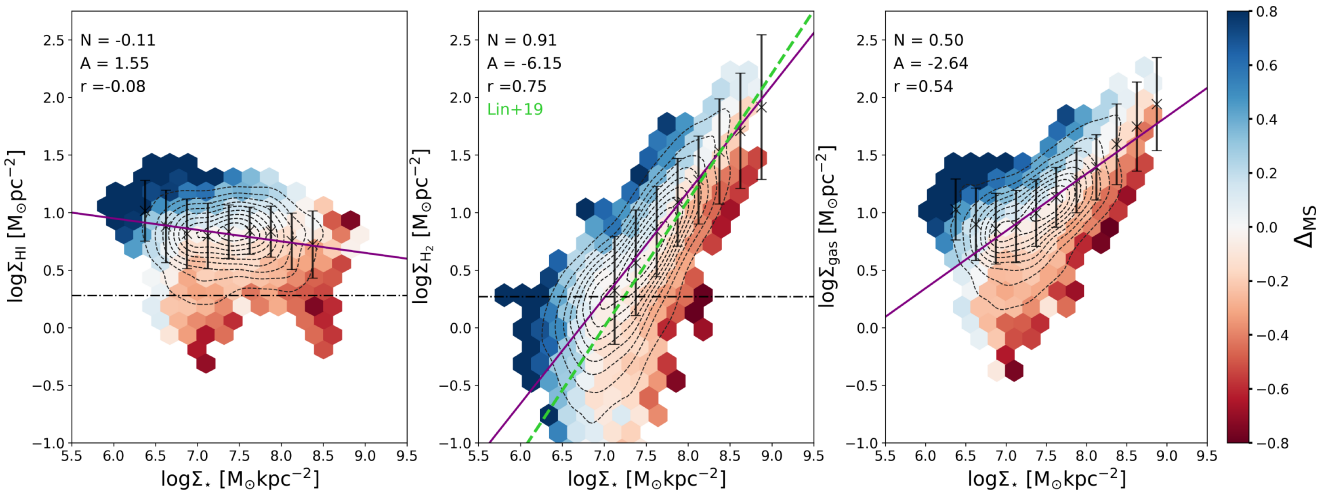

Figure 3. Distributions of the regions in the log $\Sigma_\star$–log $\Sigma_{H\,I}$ plane (left-hand panel), log $\Sigma_\star$–log Σ_{H_2} plane (central panel) and log $\Sigma_\star$–log Σ_{gas} plane (right-hand panel). Each hexagonal bin the plane has been colour coded according to the average value of Δ_{MS}, as in Fig. 2. The purple solid lines are the best-fitting relations obtained by fitting the average values of log$\Sigma_{H\,I,H_2,gas}$ in bins of log $\Sigma_\star$, as marked with black crosses; the slope (N) and intercept (A) of the best fit are written in the panels, together with the Spearman correlation coefficient r. The green dashed line in the central panel is the MGMS of Lin et al. (2019), re-scaled to a Chabrier IMF.

the molecular and total gas are consistent, within errors, with the integrated relations (e.g. Genzel et al. 2010; Kennicutt & Evans 2012; Tacconi et al. 2013; de los Reyes & Kennicutt 2019; Freundlich et al. 2019), similar to what is found when comparing the spatially resolved and integrated MS relation. The scatter of the integrated relation is instead significantly higher (e.g. 0.28 in de los Reyes & Kennicutt 2019).

Finally, we underline here that the trends observed in Fig. 2 are not driven by one or few of the galaxies in our sample, but by and large are common to all five galaxies in our sample. Slope and intercept of the log Σ_{H_2}–log Σ_{SFR} and log Σ_{gas}–log Σ_{SFR} relations are summarized in Table 2.

3.2 Dependence of gas distribution on stellar mass

As the trends shown in Fig. 2 with Δ_{MS} are related to variations of the gas content with $M_\star$, we show in Fig. 3 how the surface densities of neutral, molecular, and total gas vary as a function of $\Sigma_\star$. The left-hand panel of Fig. 3 shows that a very weak anticorrelation is found between log$\Sigma_\star$ and log$\Sigma_{H\,I}$. Indeed, when fitting the average values of log $\Sigma_{H\,I}$ in bins of log $\Sigma_\star$, the slope of the correlation is -0.11 ± 0.07. We stress that every galaxy shows a trend of decreasing $\Sigma_{H\,I}$ towards the central regions, as in the central region the high pressure favours the H I to H_2 transition and most of the gas is in molecular form, but such a decrease can be more or less pronounced from galaxy to galaxy, and does not follow a universal behaviour. Starbursting regions are preferentially located at $r > 0.5R_{25}$, where the surface density of stars falls below 10^7 M⊙ pc^{-2}, and are generally found along the spiral arms.

The relation between log $\Sigma_\star$ and log Σ_{H_2}, shown in the central panel of Fig. 3, is consistently common to all five galaxies and gives birth to a very tight correlation, the MGMS (Lin et al. 2019). The MGMS (re-scaled to a Chabrier IMF) of Lin et al. (2019) is indicated with a green dashed line in the central panel of Fig. 3 and has a slope of 1.1. To obtain the slope of our MGMS relation, we fit the average values of log Σ_{H_2} in bins of log $\Sigma_\star$, restricting the analysis to stellar surface densities where the average value of log Σ_{H_2} is above the sensitivity limit. We find

$$\log \Sigma_{H_2} = 0.91(\pm 0.29) \times \log \Sigma_\star - 6.15(\pm 2.11). \quad (4)$$

This relation has a scatter of 0.22 dex, similar to that obtained for the MS (0.23 dex), and the Spearman coefficient is the same as for the log $\Sigma_{H_2/gas}$–log Σ_{SFR} relations. We find a slope that is consistent within the error with the one of Lin et al. (2019), i.e. 1.1. The different slopes can be ascribed to different fitting procedures; indeed, if we follow the ODR method, we also retrieve a super-linear slope. Regions with the largest sSFR are located in the upper envelope of this relation; in other words, cells located above the spatially resolved MS are also located above the log $\Sigma_\star$–log Σ_{H_2} relation. This trend, outlined also in Ellison et al. (2020b), is here as significant as the one visible in Fig. 2 for the molecular KS relation.

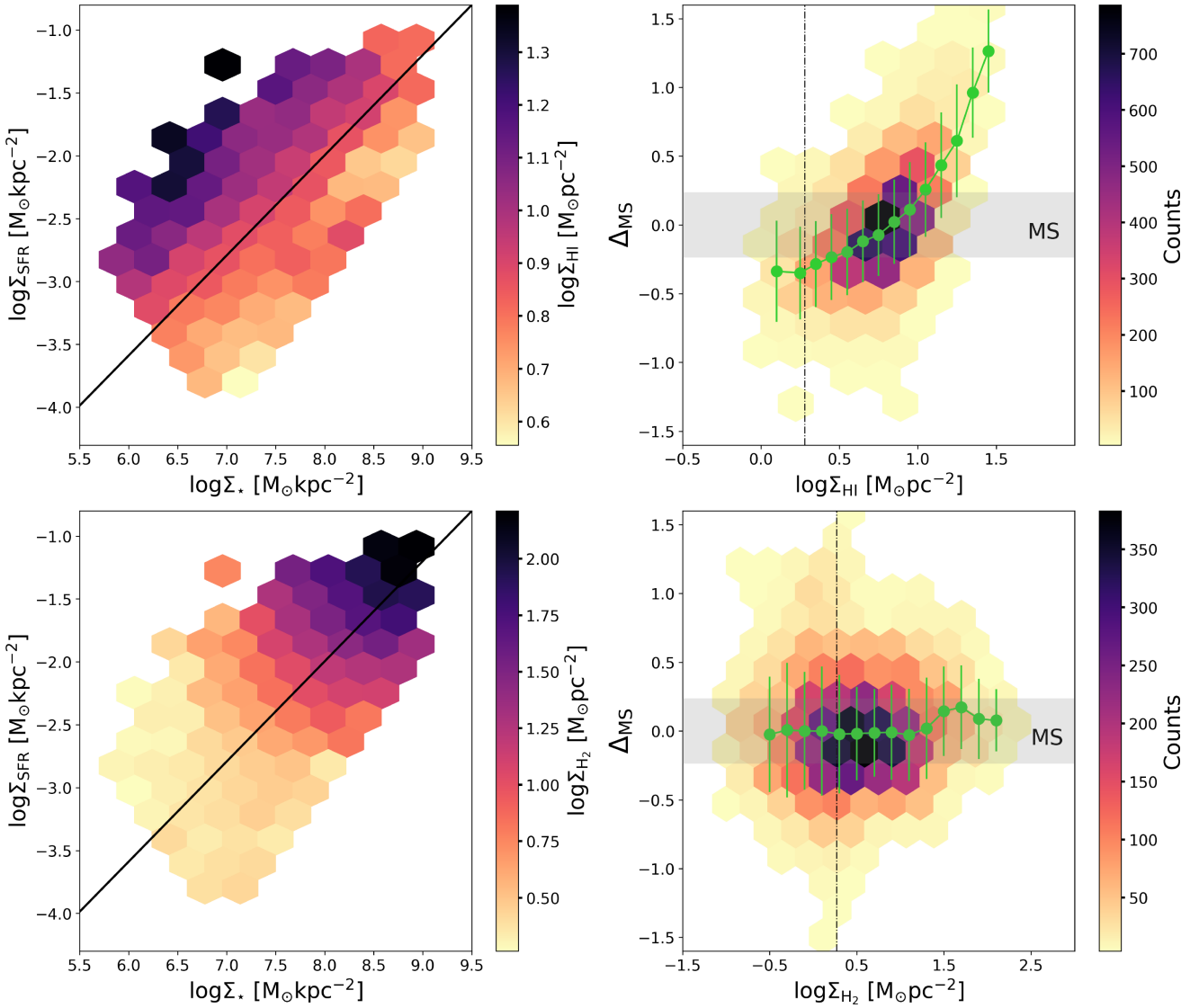

Figure 4. H I and H_2 in the log$\Sigma_\star$–logΣ_{SFR} plane. Top left-hand panel: log$\Sigma_\star$–logΣ_{SFR} plane colour coded as a function of the average value of logΣ_{HI} in each bin. The black sold line marks the location of the spatially resolved MS relation. Top right-hand panel: Δ_{MS}, as a function of logΣ_{HI}. The average values of Δ_{MS} computed in bins of logΣ_{HI} are shown in green. Each bin is colour coded as a function of the number of cells that it contains. Bottom left-hand panel: log$\Sigma_\star$–logΣ_{SFR} plane colour coded as a function of the average value of logΣ_{H_2} in each bin. The black sold line marks the location of the spatially resolved MS relation. Bottom right-hand panel: Δ_{MS}, as a function of logΣ_{H_2}. The average values of Δ_{MS} computed in bins of logΣ_{H_2} are shown in green. Each bin is colour coded as a function of the number of cells that it contains. In the right-hand panels, the grey shaded area marks the MS region.

A correlation is also apparent between log $\Sigma_\star$ and log Σ_{gas}, that is the combination of the two behaviours seen in the left and central panel of Fig. 3. At low $\Sigma_\star$ (log $\Sigma_\star \lesssim 7$), the H I tends to dominate over H_2, and the scatter of the relation is larger, while it is slightly narrower at large $\Sigma_\star$. This combined behaviour results in a slope of 0.50 ± 0.14 and an intercept of -2.64 ± 0.97, and a Spearman coefficient of 0.54. Slope and intercept of the log $\Sigma_\star$–log Σ_{gas} and log $\Sigma_\star$–log Σ_{H_2} relations are summarized in Table 2.

3.3 H I and H_2 in the $\Sigma_\star$–Σ_{SFR} plane

To further analyse the link between the atomic, molecular, and total gas and the star formation properties of a region, we show in Fig. 4 how logΣ_{HI} and logΣ_{H_2} vary across the log$\Sigma_\star$–logΣ_{SFR} plane. In the two left-hand panels of Fig. 4, we show the log$\Sigma_\star$–logΣ_{SFR} plane colour coded as a function of the average logΣ_{HI} (top) and logΣ_{H_2} (bottom) values in each bin. The spatially resolved MS is indicated with the black solid line. To compute the average value of logΣ_{H_2}, we also used values below the sensitivity limit; therefore, it is important to emphasize that H_2 is detected only for Σ_{H_2} above ~ 3 $M_\odot$ pc^{-2} that requires a $\Sigma_\star$ higher than 10^7 $M_\odot$ kpc^{-2}. On the other hand, H_2 column densities below this threshold value are hardly self-shielded and quite rare (e.g. Sternberg et al. 2014).

Interestingly, along the MS relation the average value of logΣ_{HI} is fairly constant and equal to about 7 $M_\odot$ pc^{-2} that corresponds to an H I column density of about 9×10^{20} cm^{-2}. This indicates that for cells on the MS, the radiation field is strong enough to partially dissociate H_2, and large amounts of dust-rich H I gas prevent further H_2 dissociation (Sternberg et al. 2014). As expected, Σ_{H_2} increases with increasing $M_\star$, following the MGMS relation, suggesting that the gravity dominated by stars compresses and enhances the ISM